

BASIC RESEARCH

The effects of noise-induced hair cell lesions on cochlear electromechanical responses: A computational approach using a biophysical model

Amin Saremi¹ | Stefan Stenfelt²

¹Department of Applied Physics and Electronics, Umeå University, Umeå, Sweden

²Department of Biomedical and Clinical Sciences, Linköping University, Linköping, Sweden

Correspondence

Amin Saremi, Department of Applied Physics and Electronics, Umeå University, 901 87 Umeå, Sweden.

Email: amin.saremi@umu.se

Funding information

DFG Cluster of Excellence, Grant/Award Number: EXC 1077/1 "Hearing4all", University of Oldenburg, Germany; Hörselskadades Riksförbund (HRF); Swedish Research Council, Grant/Award Numbers: 2017-06092, 349-2007-8654

Abstract

A biophysically inspired signal processing model of the human cochlea is deployed to simulate the effects of specific noise-induced inner hair cell (IHC) and outer hair cell (OHC) lesions on hearing thresholds, cochlear compression, and the spectral and temporal features of the auditory nerve (AN) coding. The model predictions were evaluated by comparison with corresponding data from animal studies as well as human clinical observations. The hearing thresholds were simulated for specific OHC and IHC damages and the cochlear nonlinearity was assessed at 0.5 and 4 kHz. The tuning curves were estimated at 1 kHz and the contributions of the OHC and IHC pathologies to the tuning curve were distinguished by the model. Furthermore, the phase locking of AN spikes were simulated in quiet and in presence of noise. The model predicts that the phase locking drastically deteriorates in noise indicating the disturbing effect of background noise on the temporal coding in case of hearing impairment. Moreover, the paper presents an example wherein the model is inversely configured for diagnostic purposes using a machine learning optimization technique (Nelder–Mead method). Accordingly, the model finds a specific pattern of OHC lesions that gives the audiometric hearing loss measured in a group of noise-induced hearing impaired humans.

KEYWORDS

auditory nerve, auditory periphery, cochlear electromechanics, cochlear models, Nelder–Mead optimization method, noise-induced hearing loss

1 | INTRODUCTION

Hearing loss affects approximately one in five, globally.¹ One common cause for a hearing loss is exposure to high sound levels. It has been demonstrated that inner-ear stereocilia micromechanics change during exposure to intense stimulation which may recover shortly after the stimulation ends.^{2–4} However, if the stimulation is too intense or the exposure duration is too long, it may lead to permanent damage or even the death of the outer hair cells (OHCs) and/or the inner hair cells (IHCs) through either apoptosis or necrosis processes.^{3,5,6} This clinical condition is known as

This is an open access article under the terms of the [Creative Commons Attribution-NonCommercial-NoDerivs](https://creativecommons.org/licenses/by-nc-nd/4.0/) License, which permits use and distribution in any medium, provided the original work is properly cited, the use is non-commercial and no modifications or adaptations are made.

© 2022 The Authors. *International Journal for Numerical Methods in Biomedical Engineering* published by John Wiley & Sons Ltd.

noise-induced hearing loss (NIHL), which is common among construction workers, musicians, military staff, and hunters.⁷ Despite this, routine clinical methods do not clearly pinpoint and differentiate the physiological roots of these impairments.^{8–10}

The negative effects of noise exposure on mammalian cochlear physiology have been extensively recorded and studied in animals (e.g., References 2, 3, 5, 10, 11). However, in humans, it is impracticable to instantly assess the cochlear status *in vivo*. Therefore, in absence of direct measurements, it is necessary to develop computational models to facilitate our understanding of the underlying mechanisms causing the observed NIHL in humans.

A large number of computational auditory models have been developed as mathematical frameworks to quantitatively describe the signal processing in the human hearing system. These models reproduce key features of the human sound coding such as critical bands, excitation patterns, and active level- and frequency-dependent cochlear amplification (see Meddis and Lopez-Poveda¹² for a review). The main idea behind these functional (phenomenological) models is to reproduce the overall psychoacoustic outcome of the auditory system using different combination of linear and nonlinear computational elements, that is, filter banks and compressors, without directly linking these elements with structural details and subprocesses at the cellular level. Saremi et al.¹³ analyzed the performance of several publicly available auditory models in reproducing the forth mentioned physiological and psychoacoustic features of the human auditory periphery. In recent years, a new line of modeling has emerged which aims at incorporating biophysical details of cellular structures to establish a link between cochlear signal processing and the underlying biological mechanisms (e.g., References 14–16).

The aim of this study is to use a biophysically inspired model of the mammalian cochlea to better understand and differentiate the underlying mechanisms, and consequences of specific cochlear lesions associated with noise-induced lesions on the human peripheral auditory functions. A key interest is to simulate the consequences of specific hair cell lesions based on experimental studies and to numerically differentiate between the contributions of OHC lesions versus IHC lesions in generating the observed outcomes. The peripheral auditory functions that are investigated in this analysis include the hearing thresholds, cochlear nonlinear response growth, cochlear frequency tuning and the phase locking of the AN spikes. The predictions of the model are evaluated by comparing to relevant experimental data from animal and human studies, whenever available.

The model is also used to associate a specific OHC lesion pattern to a given audiometric hearing loss as an example to show the model's potentials in diagnosing the biophysical origins of cochlear hearing loss. This is accomplished by a numerical optimization algorithm based on Nelder–Mead simplex¹⁷ which is applied on the model to find a specific configuration of OHC lesions that closely yields the given audiogram measured in a group of hearing-impaired individuals with documented history of noise exposure.

2 | METHOD

2.1 | Modeling methods

Saremi and Stenfelt¹⁵ introduced a detailed biophysically motivated computational model of the mammalian cochlear mechanics. The model performed well in a comparative study of seven human cochlear mechanics models¹³ which analyzed the overall success of these models in reproducing several key features of the human cochlear functions by quantitatively comparing the output predictions of these models to a large set of available physiological data recorded from mammalian cochleae as well as translational psychoacoustic data from human clinical studies.

The original biophysical model of Saremi and Stenfelt¹⁵ was devised to simulate the cochlear mechanical vibrations and did not include the forthcoming sensory IHC and auditory nerve (AN) stages. Therefore, to enable simulating the neuronal activity on the AN fibers, the output of the model is connected to a biophysical model of the human IHC by Lopez-Poveda and Eustaque-Martin,¹⁸ and a computational auditory-nerve spike generator by Zilany et al.¹⁹

Figure 1 depicts the model stages in a bottom-up manner representing the entire mammalian auditory periphery extending from the outer ear to the AN fibers. The outer-middle ear (OME) stage is a transfer function that has been derived according to the measurements by Goode et al.²⁰ This approximation of the OME functionality is based on the assumption that the OME components behave linearly within the range of the auditory intensities and thus the OME can be represented by a linear finite impulse response (FIR) filter. The sound intensities used are not too high to provoke the stapedius reflex which can challenge the linearity assumption.

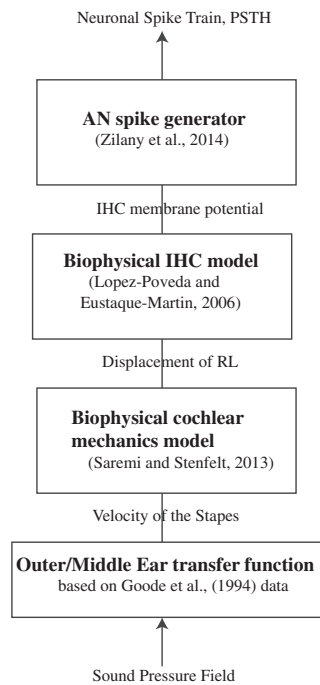


FIGURE 1 A bottom-up view of the modeling stages used in this study. The model comprises a physiologically based transfer function for the outer and middle ear, a biophysical model of the cochlear electro-mechanics, a biophysical model of the inner hair cell (IHC) and a computational representation of the auditory nerve (AN) synapse. The input and output of each stage is also shown in the figure. Each stage is described in [Appendix](#)

The cochlear mechanics stage is a biophysical lumped-element electromechanical model developed by Saremi and Stenfelt,¹⁵ which consists of a cascade of resonators whose parameters were derived from physiological measurements inside human and other mammalian cochleae. Figure [A1A](#) shows a single cochlear partition of this model together with its longitudinal coupling to the preceding partition, while Figure [A1B](#) illustrates the model's overall schematic. This stage of the model generates mechanical responses of the cochlear structures such as the displacement of the basilar membrane (BM), reticular lamina (RL), and tectorial membrane (TM).

The IHC stage used here is a biophysical lumped-element model developed by Lopez-Poveda and Eustaque-Martin.¹⁸ The model consists of cell-level parameters such as the endocochlear potential (EP), capacitance and conductance of the cell portions, and the mechanical sensitivity of the potassium channels. The input to the model is the deflection of the IHC stereocilia and the output is the IHC membrane potential.

The auditory synapse stage (AN spike generator) is based on the parameters reported by,¹⁹ according to the time-varying three-store diffusion synapse model. The current analysis includes only high spontaneous rate (HSR) fibers that are believed to be responsible for the neuronal coding of the low-intensity and mid-intensity sounds up to approximately about 30 dB above the hearing threshold.¹⁹ The three main stages of the model (Cochlear mechanics, IHC, and AN) are described in more details and their corresponding source codes are linked in [Appendix](#). If necessary, the input signals to each stage were scaled and prepared before feeding into the stage according to the specifications of the corresponding model, to achieve reasonable output signals.

2.2 | Assessing the characteristics of the peripheral auditory coding

2.2.1 | Definition of neuronal hearing threshold and hearing loss

The hearing thresholds on the AN are assessed by exciting the outer ear by a pure tone at 0 dB SPL and then increasing the level until a significant increase in the firing rate of the HSR AN fibers is observed.⁵ The OME filter stage is fed by the sound stimuli. The output of the OME filter determines the stapes vibration that excites the cochlear mechanical

model which, in turn, generates the displacement of the RL as output. The displacement of the RL is fed into the IHC model that yields the membrane potential of the IHC. Finally, the AN synapse model processes the IHC membrane potential and gives the spikes on the AN fibers, in form of the post-stimulus time histograms (PSTH) with the bin size of 0.4 ms. Due to the probabilistic nature of the neuronal activity, the AN processing is repeated 50 times for every case and the results are averaged. The threshold is then defined as the minimum tone level that causes a 10% increase above the spontaneous rate (i.e., the firing rate in absence of any stimulus) of the HSR fibers.

Lieberman and Dodds⁵ defined the hearing thresholds in their measurements based on an earlier work²¹ as the input sound level that increases the firing rate of the HSR AN by 10 spikes/s over its spontaneous rate (see figure 1 of Lieberman²¹). Zilany and Bruce²² used the same definition for estimating the neuronal hearing thresholds in their model (see figure 4A of Zilany and Bruce²²). We used the 10% increase above the spontaneous rate instead to mark the hearing thresholds. This percentage-based definition, given that the baseline spontaneous rate is typically slightly over 100 spikes/s in our simulations, is close to the definition in References 5, 22. However, choosing a percentage-based criterion for defining threshold has the advantage of minimizing the numerical noise in our simulation which originates from probabilistic fluctuations in the baseline spontaneous rate.

The hearing thresholds are estimated based on the above neuronal definition for CFs from 0.3 to 10 kHz with steps of 100 Hz. The hearing thresholds are also estimated for the pathological conditions where OHCs and/or IHCs are selectively damaged. For these cases, the pathological thresholds are compared with the healthy thresholds to estimate the corresponding hearing threshold elevations. The hearing loss is defined as the amount of hearing threshold elevation in these pathological cases.

2.2.2 | Cochlear nonlinear response growth: The cochlear mechanical compression

Several studies have shown that as the level of an incoming tone is increased, the amplitude of the BM mechanical vibration at the corresponding characteristic frequency (CF) site also increases; however, this growth is nonlinear for a wide range of input levels.^{23–25} In other words, the function that relates the amplitude of the mechanical response at the CF to the amplitude of the stimuli, known as the “input/output (I/O) function” depicts nonlinear (compressive) growth.

The I/O nonlinearity is commonly linked to the status of the OHCs and its active mechanisms. This link is well established as many studies have indicated that the I/O nonlinearity disappears as the “active” cochlea transforms to a passive one due to the damages to the OHCs.^{24,26} The IHCs, on the other hand, are believed not to have any direct role in the nonlinearity of the I/O functions.^{24,25,27}

The cochlear input/output (I/O) functions are defined as the amplitude of the RL vibration at the CF, as a function of the stimulus intensity. The model predictions for the I/O functions can be calculated at any given CF, by feeding a 100-ms sinusoid signal (including a 5-ms rise and decay to minimize the spectral splatter) to the models, with levels between 10 and 100 dB SPL. The output is estimated by measuring the root mean square (RMS) of the vibration amplitude at the corresponding CF. In the current study, the I/O functions are estimated at two CFs, 500 Hz (apical area) and 4 kHz (basal area). The simulated I/O functions at 0.5 and 4 kHz are compared with the experimentally estimated I/O functions in the comparable apical region of the chinchilla cochlea²³ and in the basal region of the guinea pig cochlea.²⁶

2.2.3 | Neuronal tuning curves: The cochlear spectral processing

The frequency selectivity of the mammalian ears is often assessed by obtaining the “tuning curves.”^{28,29} The tuning curve is estimated at any given CF by invasively measuring the neuronal firing thresholds on the AN as a function of the frequency (e.g., Lieberman and Dodds⁵). In the human ears, the frequency selectivity is indirectly estimated by psychophysical tuning curves (PTCs) using psychoacoustic masking paradigms (e.g., Sek et al.²⁹).

The sharpness of the tuning curves in healthy ears manifest the high frequency selectivity of the healthy auditory system.^{28,30} This remarkable tuning critically depends on the functionality of both OHCs and IHCs. In case of damages to the OHCs, the tuning curve is broadened and shallower and the tip of the tuning curve is elevated (see figure 14 of Lieberman, and Dodds⁵). The profound IHC damage, however, precludes the transformation of the cochlear vibration to the neuronal activity entirely, leading to a “dead region.”^{6,29,30}

The AN tuning curves are approximated at the CF of 1 kHz by estimating the thresholds at this CF in response to tones at probe frequencies from 0.2 to 1.5 kHz. The thresholds form a tuning curve that is then compared to the tuning curve measured on the HSR fibers in a comparable region of the healthy cat cochlea (see figure 4 of Liberman and Dodds⁵).

2.2.4 | Neuronal phase locking: The cochlear temporal processing

Phase locking refers to the firing of the neurons at a certain phase of the stimulus and is an important temporal feature of the auditory peripheral system.^{6,31–33} Phase locking is generally assessed by calculating the “vector strength” from the phase histogram (i.e., a histogram that shows the number of AN firings at a given phase of the stimulus).³² The vector strength yields “1” in case of a perfect phase locking whereas a vector strength of “0” indicates a completely random temporal relation between the stimulus and the AN response.³²

The AN spikes are generated from the PSTH using a refractory period of 0.75 ms. The spike train is compared with the stimulus and each spike (i) is assumed as a unit-long vector with a phase of θ_i between 0 and 2π . The phase of the spike (θ_i) is considered equal to the phase of the stimulus at the same sample. A phase histogram is then formed which determines the number of spikes at all phases from 0 to 2π . The mean phase relation between the stimulus and the AN discharge is calculated according to Equation (1a) where k equals zero or one to limit the mean phase between 0 and 2π . The vector strength (r) is estimated from the phase vectors (θ_i) according to Equation (1b) below by.³¹

$$\theta = \text{Arctan} \left(\frac{\sum_i \sin(\theta_i)}{\sum_i \cos(\theta_i)} \right) \mp k\pi \quad (1a)$$

$$r = \sqrt{\left(\sum_i \sin(\theta_i) \right)^2 + \left(\sum_i \cos(\theta_i) \right)^2} \quad (1b)$$

The vector strength (r) is estimated in response to 50 dB SPL tones at frequencies from 0.3 to 4 kHz, for the model using Equation (1b). The level of the tones was chosen 50 dB SPL to be adequately above the hearing thresholds. The results are compared to the experimentally estimated phase locking of the cat HSR AN fibers.³¹ In addition, the vector strength is calculated in response to tones when the OHCs and IHCs are damaged at specific regions. This is done both in quiet and in the presence of a 20-kHz wideband background noise with its RMS level set 15 dB higher than the level of the tone. This is similar to the experiment by Henry and Heinz³⁴ where they recorded the AN phase locking on the HSR AN fibers inside noise-damaged chinchilla cochleae.

2.3 | Simulating noise-induced pathologies

2.3.1 | OHC Pathologies

Lim et al.³ exposed a group of mice to band-limited white noise (0.3–10 kHz) and quantitatively investigated the morphological changes in the OHCs along the cochlear length due to the noise exposure. Their results showed that, 1 day after the noise exposures, the OHCs were almost intact in the most apical region of the cochlea but the percentage of the intact cells significantly decreased to 40% in the basal region. To simulate the effect of the OHC losses on the hearing threshold, the magnitude of the OHC gain (equation 7 of Saremi, and Stenfelt¹⁵) in the corresponding partitions is multiplied by the integrity rates reported in figure 2 of Meaud and Lemons³ leading to elevated hearing thresholds. These model predictions are compared with the threshold elevations reported at four frequencies: 4, 8, 16, and 32 kHz in the mice (see figure 5 of Lim et al.³), corresponding to the CFs 1, 2, 4, and 8 kHz in humans based on the Greenwood functions.³⁵

The OHC pathology reported by Lim et al.³ is one of the many possible configurations of OHC lesions along the cochlear duct. To investigate other possible distributions of noise-induced OHC pathology, a theoretical configuration is simulated to illuminate the concept: The cochlea is divided into three regions with equal lengths: basal, middle and apical. The OHCs in the basal region are assumed to be totally dead. This assumption is in line with the experimental observations suggesting that the hair cells located in most basal regions of the mammalian cochleae are significantly

more vulnerable to acoustic overstimulation than the hair cells located in apical areas.^{3,7} Furthermore, half of the OHCs located in the middle 1/3 of the cochlear length are assumed dead (50% integrity). Finally, the most apical OHCs are assumed to be totally intact and fully active (100% integrity).

This specific distribution of the OHC pathologies is a conceptual configuration to represent a theoretical distribution of noise-induced OHC lesions along the cochlear duct. The magnitude of the OHC gain in the corresponding cochlear partitions were scaled accordingly and the hearing thresholds were estimated for this condition at CFs from 0.1 to 10 kHz. The associated hearing losses were compared with the audiograms that were categorized as “sensory” based on the subjects’ medical history in a data base of 188 human subjects (table 2.1 of Schmiedt³⁶).

Also of interest is the effect of profound OHC death on the cochlear mechanical compression and nonlinear response growth. This is done by setting the magnitude of the OHC gain to zero in all cochlear partitions. The resulting I/O curves are then normalized and compared to the I/O functions measured in postmortem cochleae (figure 16 of Ruggero et al.²⁴) where the active role of the OHCs is absent due to the death of the animal.

2.3.2 | IHC Pathologies

Wang et al.²⁷ used Carboplatin to selectively damage the IHCs in chinchilla cochleae while keeping the OHC structures intact. They measured the CAP (compound action potential) threshold elevations associated with the selective IHC pathologies. The IHC pathologies can be simulated by either scaling the IHC membrane potential in the model² or by increasing the resistance attributed to the IHC stereocilia cation channel.² Here, we scale the IHC membrane potential in corresponding cochlear partitions to simulate the reported IHC pathologies (figure 1A of Wang et al.²⁷) in line with the method used by Zilany and Bruce.²² The hearing thresholds are then estimated for this condition and compared to the hearing thresholds reported by Wang et al.²⁷ at the corresponding CFs.

2.3.3 | Mixed OHC/IHC pathologies

Liberman and Dodds⁵ obtained tuning curves in cats with selective noise-induced damages to their OHCs and IHCs structures. One of the several reported configuration with combined IHC and OHC pathologies (figure 4 of Liberman and Dodds⁵) is considered here while similar analysis can be performed at other CFs. This specific configuration includes regional IHC damages that peak to ~50% at the CF of 2 kHz, as well as less severe OHC damages in the same cochlear region. This CF in cat cochlea corresponds to the CF of about 1 kHz in human cochlea according to the Greenwood functions.³⁵ The IHC and OHC pathologies are translated to the human frequencies and simulated as explained in the previous sections. The tuning curve is simulated accordingly for this condition and compared with the measured tuning curve reported in figure 4 of Liberman and Dodds.⁵ Furthermore, the OHC and IHC contributions to the simulated tuning curve are differentiated by the model to investigate how much the OHC and IHC pathologies separately account for the observed changes in the tuning curve.

2.4 | Evaluating the model predictions

While the human cochlea is inaccessible in vivo, data from animal studies are commonly extrapolated to humans under the fundamental assumption that all mammalian cochleae share similar mechanics at proportionally similar cochlear regions (see Robles et al.²⁵ for a review). For example, the cochlear location at 33% of the total cochlear length from the base is assumed to be tuned to 4 kHz in humans (figure 1 of Greenwood³⁵). This specific location (i.e., 33% of the total length from base) is tuned to about 15 kHz in guinea pigs (figure 4 of Greenwood³⁵). Accordingly, we compared our model predictions at CF of 4 kHz in humans to the CF of 15 kHz in Guinea pig cochleae, which both point to the same proportional location in the cochlear duct. The precision of the cochlear place-frequency map that is commonly used to extrapolate animal data to corresponding cochlear locations in humans remains questionable. However, experimental comparisons of BM mechanics for several mammalian species have quantitatively confirmed the remarkable similarity of the electromechanical responses at proportional regions of the cochleae and supported the validity of translating data across mammalian species.²⁵

To quantitatively evaluate the model predictions with regard to the given experimental references, mean absolute errors (MAEs) were calculated according to Equation (2) below, where i denotes the index varying from 1 to the length of the related experimental data set (N). M_i and R_i are the model prediction and the experimental data samples in the same units, respectively.

$$\text{MAE} = \frac{\sum_{i=1}^N |M_i - R_i|}{N} \quad (2)$$

The MAEs are regarded as a measure of how close the model predictions are to the corresponding experimental data.¹³

2.5 | Using the model for diagnosing NIHL

Standard air-conduction tone audiometry is still the most common method practiced at hearing clinics around the world for assessing the severity of human hearing loss.^{7,8} Audiometry is a behavioral test that assesses the hearing loss by estimating the overall hearing threshold elevation without pinpointing its underlying cause.^{8–10,37}

In case of NIHL, the main cause of the observed hearing threshold elevations is believed to be OHC lesions³⁷ although other factors could contribute too.^{3,4,7,10,11} Therefore, we assume that, based on some other tests and estimates, it has been established that the origin of a given noise-induced audiometric hearing loss is the OHC lesions. This is a reasonable assumption in case of NIHL.³⁷ The model is then used to predict the extent and severity of the corresponding OHC lesions that could have caused the observed audiometric hearing loss. Other factors, such as IHC deficiencies and EP reduction, can be similarly added to this analysis. However, to keep the simulations simple and computationally robust, we solely focus on OHCs in this study.

2.5.1 | Data collection

A group of seven male individuals aged between 30 and 55 years old (mean = 49.5, SD = 6.6) with a well-documented history of NIHL were recruited at the hearing clinic of the Linköping university hospital. Candidates with any of these conditions were excluded from the study (exclusion criteria): (1) severe tinnitus, or hyperacusis, (2) chronic cardiovascular diseases, diabetes requiring medicine, hypertension requiring medicine, (3) asymmetric hearing loss, (4) autoimmune disease, (5) exposure to ototoxic drugs, and (6) cancer diagnosis.

Standard air-conduction tone audiometry was performed on the NIHL participants at frequencies between 0.125 and 8 kHz. Hearing thresholds at each measurement frequency were averaged. Moreover, standard Swedish hearing-in-noise test (HINT)³⁸ was performed on this group of NIHL participants. All NIHL participants were native Swedish speakers. The Swedish HINT consists of everyday sentences in background noise that are used in an adaptive process to assess the speech recognition threshold. The HINT score estimates the amount of speech-to-noise ratio (SNR) that is required by an individual to be able to perceive half of the sentences correctly. Swedish HINT was also performed on 20 normal-hearing native Swedish speakers to provide a baseline for comparison.

The data collection was approved by the Regional Ethical Committee, Östergötland County, Sweden.

2.5.2 | Numerical optimization process

The average audiogram obtained in the NIHL group is used as an input to an optimization method. The optimization task is to find a pattern of OHC lesions that could closely yield the given audiogram. The model consists of 100 OHC partitions from base to apex. Simplex-based numerical optimization methods can only be efficiently implemented on few variables, typically on less than 20 variables.¹⁷ Therefore to reduce the number of variables and the consecutive computational complexity, we assign one variable to every 5 cochlear partitions resulting in total of 20 variables for the optimization. After the optimization method is applied, the results are interpolated back to 100 partitions.

The optimization process starts with an initial guess for the input variables. From a computational perspective, it is necessary to set realistic values to allow the optimization process to start from a feasible point. Since the most basal

OHCs are likely to be damaged due to noise exposure^{3,7} we set the initial guess to zero (totally dysfunctional) for the first three OHC variables, while the last six variables (most apical partitions) were initially set to one (totally functional); the other OHC variables which are in the middle of the cochlear duct were initially set to 0.5 (half functional). The algorithm starts by feeding the initial guess into the cochlear mechanics model¹⁵ and calculate the cochlear amplification loss from the output of the model in dB at all 100 partitions (denoted by \widehat{H}_{ji}) where i represents the cochlear partition (ranging from 1 to 100) and j represents the current iteration number ($j = 0$ when feeding the initial guess). A cost function is then estimated based on the least mean square error (LMSE) shown in Equation (3) where H_i is the hearing threshold elevations in dB at the cochlear partition number i , according to the measured audiogram.

$$\text{Cost function at } j\text{th evaluation} = \sqrt{\frac{\sum_{i=0}^{100} (\widehat{H}_{ji} - H_i)^2}{100}} \quad (3)$$

The optimization algorithms forms a simplex and seeks to improve the initial guess so that the cost function minimizes at the next iteration and thereby the output of the cochlear model approaches the given audiogram. We used the bound *fminsearch* instruction in MATLAB that is based on the Nelder–Mead method (also known as downhill simplex method) which is a common numerical method applied to multi-variable nonlinear optimization problems.¹⁷ Accordingly, a simplex is formed and a local minimum of the cost function is estimated at each consecutive function evaluation and the variables are updated to move the simplex downwards toward a local minimum. The method bounds the input variables to vary between zero (fully dysfunctional) and one (fully functional). The maximum number of searches (cost function evaluations) was set to 1000. The source code for this analysis is available on GitHub.³⁹

3 | RESULTS

The arbitrary number of cochlear partitions is chosen to 100 ($N = 100$) and the simulations are implemented according to the bottom-up pathway shown in Figure 1, using MATLAB[®] and C.

3.1 | Neuronal hearing thresholds and hearing loss

Figure 2 illustrates the hearing thresholds estimated in the healthy condition, according to the neuronal activity on the HSR fibers of the AN. The solid line in Figure 2 shows the hearing thresholds simulated at the CFs from 0.3 to 10 kHz by our model which corresponds to the cochlear regions between 0.85 and 0.15 of the total length from base. This cochlear region translates to the CFs from 0.8 to 40 kHz in the cat cochlea, according to the Greenwood functions.³⁵ The crosses depict some of the thresholds recorded at corresponding CFs on the HSR fibers of the healthy cat cochlea by Liberman and Dodds (see figure 3A of Liberman and Dodds⁵ for the original data). Figure 2 indicates that the predictions of the model deviate 2.3 dB from the cat data in MAE, according to Equation (2).

Figure 3A illustrates the selective IHC pathologies along the chinchilla cochlea due to administration of Carboplatin as reported by figure 1A of Wang et al.²⁷ Figure 3B shows the hearing thresholds for this specific IHC pathology (crosses), as well as the hearing thresholds for the healthy cochlea (solid gray line). Comparison of these two curves indicates that the hearing threshold elevation is almost negligible at CFs below 2 kHz and increases to only 4 dB for higher CFs (from 2 to 10 kHz). This is consistent with the CAP thresholds reported by figure 2B of Wang et al.,²⁷ shown by circles, which also indicate a small amount of threshold elevations caused by this specific IHC pathology. The model prediction (crosses) deviates 0.42 dB in MAE from the corresponding data (circles)

Figure 4A shows the OHC integrity along the cochlear duct interpolated, using the MATLAB function *interp1*, from the experimental data recorded in the mice cochlea after noise exposure (figure 3 of Lim et al.³). Figure 4B depicts the simulated hearing loss, estimated from the hearing threshold elevations for CFs from 0.1 to 10 kHz. The model predicts a hearing loss of 22 dB at 100 Hz which increases to its maximum of 53 dB at 4 kHz and then recovers at higher frequencies. The model predictions (solid line) can be compared with the hearing loss calculated from the recorded auditory brainstem response (ABR) threshold elevations (figure 4 of Lim et al.³) depicted by circles, showing an MAE

deviation of 4.25 dB which suggests that the model reproduces the measured data relatively closely. Although ABR hearing thresholds could be different from audiometric thresholds, there is a very high correlation between them⁴⁰

Figure 5A illustrates the OHC integrity along the cochlear length in a theoretical scenario of noise-induced OHC lesion. Figure 5B Shows the hearing loss caused by this specific distribution of damaged OHCs, estimated according to the hearing threshold elevations. Figure 5B Demonstrates a mild hearing loss at low frequencies followed by a sharply sloping loss for frequencies above 1.5 kHz which reaches a maximum of 82 dB at 4.1 kHz and slightly improves thereafter

Schmiedt³⁶ categorized audiograms obtained from 188 adult human subjects into five groups based on the subjects' personal history and behavioral patterns (table 2.1 and figure 2.13 of Schmiedt³⁶). The circles in Figure 5B show the average hearing thresholds at 6 audiometric frequencies (0.25, 0.5, 1, 2, 4, and 8 kHz) for the “sensory category” while the error bars represent the range of the expected values corresponding to the dashed area in the “sensory” panel of figure 2.13 in Schmiedt.³⁶ Although, the model predicts a steeper and a larger hearing loss at 4 kHz, the model prediction shows a reasonable match with the illustrated clinical data. Figure 5 indicates that the model is capable of associating an observed audiometric pattern with specific hair cell lesions that might have caused it.

3.2 | Cochlear mechanical compression

Figure 6A shows the I/O function simulated at the CF of 500 Hz (solid line) together with experimental I/O data (crosses) recorded in the chinchilla cochlea at an apical region tuned to 800 Hz.²³ This region at 25% of the cochlear length from the apex is tuned to 500 Hz in humans.³⁵ Both data sets have been normalized with respect to the reference point (10 dB output at 10 dB input) to depict the nonlinear response growth. The deviation between model prediction (solid line) and the experimental data (crosses) is 6.5 dB in MAE.

Furthermore, the I/O function is simulated for the passive (postmortem) condition where the OHC contribution is totally absent and compared with the corresponding postmortem data.²⁴ This I/O curve is shown by a dashed line and depicts a totally linear response growth which indicates the absence of the OHC active mechanisms (see Robles and Ruggero²⁵ for a review).

Figure 6B illustrates the I/O function at the CF of 4 kHz (solid line) along with the experimental data (crosses) recorded in the guinea pig cochlea²⁶ at a basal region tuned to 16 kHz. This region at 33% of the cochlear length from the base is tuned to 4 kHz in humans according to the Greenwood frequency-position map.³⁵ Both of these I/O functions have been normalized with respect to the reference point (10 dB input, 10 dB output). The deviation between model prediction (solid line) and the experimental data (crosses) is 7.8 dB in MAE

Furthermore, the I/O function is simulated for the postmortem condition (dashed lines) and is shown along with the I/O function experimentally obtained from a postmortem chinchilla cochlea (figure 16 of Ruggero et al.²⁴), shown by a gray line. The simulated I/O function and the experimental one both show a totally linear behavior with a similar

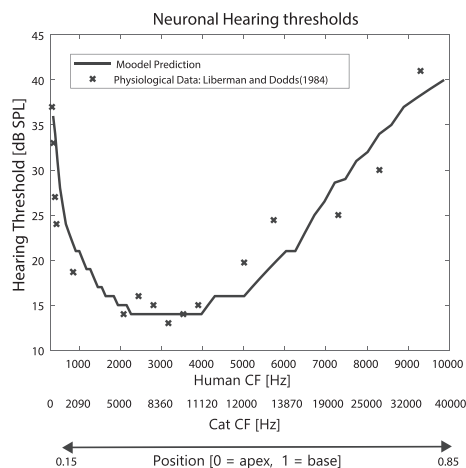


FIGURE 2 The hearing thresholds estimated on the auditory nerve (AN) fibers for the characteristic frequencies (CFs) ranging from 0.3 to 10 kHz

slope. The hearing threshold occurs at 13 dB SPL in a healthy cochlea. This is highlighted by a dashed gray line. The distance between the healthy I/O function and the postmortem I/O function (shown by the arrow) represents the amount of reduction in the maximum cochlear gain caused by the OHC death. The arrow in Figure 6B indicates a 53-dB hearing loss at 4 kHz due to the assumed OHC impairment.

3.3 | Tuning curves

Figure 7A illustrates the distribution of the OHC and IHC pathologies along the cat cochlea due to noise exposure at CFs from 0.8 to 5 kHz as reported by figure 4C of Liberman and Dodds.⁵ Based on the Greenwood function, these pathologies are distributed from ~15% to 50% of the cochlear duct from the apex which is approximately tuned to 0.3–2 kHz in human cochleae. The OHC/IHC contributions are scaled in corresponding cochlear partitions according to the distribution of the pathologies shown in Figure 7A. The tuning curve is then simulated by the model for this specific case of combined OHC/IHC lesions as well as for the healthy condition at the CF of 1 kHz shown by the solid line and the dashed line in Figure 7B, respectively.

To make the visual comparison easier, Figure 7B also illustrates the corresponding physiological tuning curves measured by Liberman and Dodds⁵ for these two specific cases. The crosses show the measured data for the healthy case while the circles show the tuning curve data for the OHC/IHC damaged case. These experimental data sets have been reproduced from figure 4, (top panel) of Liberman and Dodds.⁵ The comparison of the model prediction (solid line) with the measured physiological data (crosses) in Figure 7B shows that the model successfully reproduces the tuning curve for the healthy case around the CF and the higher-frequency side while showing larger deviations in the lower-frequency tail. The MAE deviation between the two curves is calculated 6.3 dB based on Equation (2). The simulated

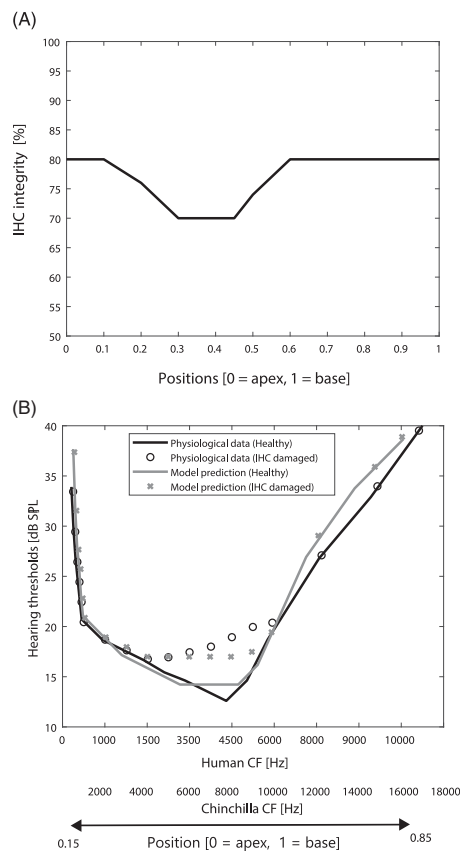


FIGURE 3 (A) The distribution of the inner hair cell (IHC) damages along the cochlea reported by figure 1A of Wang et al.²⁷ (B) The model prediction of the hearing thresholds for the healthy case and the case with the IHC pathologies in panel (A), together with the experimental data (Fig. 2B of Wang et al.²⁷)

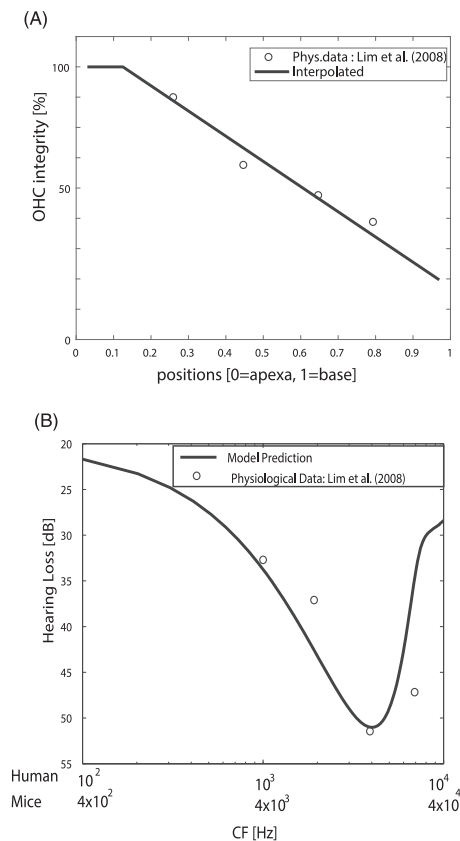


FIGURE 4 (A) The distribution of the outer hair cell (OHC) damages along the cochlea as reported by figure 2 of Lim et al.³ (B) The model prediction of the hearing loss for the configuration shown in panel (A). The circles are taken from the observed threshold elevations after the noise exposure (figure 5 of Lim et al.³)

lower-frequency tail is relatively shallower than the one based on the measured data leading to 19 dB difference at the lowest frequencies.

The simulation of the tuning curve associated with the combined OHC/IHC pathologies (dashed line) shows that the tip of the curve is elevated by around 33 dB and is shifted toward lower frequencies by about 100 Hz. This is similar to the corresponding physiological measurements (circles) where the vertical elevation of the tip of the tuning curve is ~ 40 dB and the horizontal shift is 200 Hz in cat cochleae. This elevation of the tuning curve is linked to the hearing threshold elevation at the CF.^{29,30}

The tuning curves associated with the combined OHC/IHC lesions (circles and the dashed line) are flatter than the healthy ones. This indicates a poorer frequency selectivity of the cochlea due to the sensory damages.^{6,29,30} This is in line with the human clinical data where a broadening of the psychoacoustic tuning curve is observed in humans with hearing impairment, for example, Sek et al.²⁹

An important analytical task that the model can do beyond the experimental data is to quantitatively distinguish between the IHC and OHC contribution to the observed changes in the tuning curve. This is accomplished by simulating the tuning curve for only IHCs damaged (Figure 7A upper panel) versus only the OHCs damaged (Figure 7A lower panel). These tuning curves are shown by two gray lines in Figure 7B. The tip of the tuning curve associated with the OHC-damages is elevated by 25 dB which indicates a 25-dB OHC-related hearing loss. The tails of this tuning curve are also broadened on both lower and higher frequency sides of the curve.

The tip of the tuning curve associated with the IHC-damages, however, is elevated only 8 dB indicating an 8-dB IHC-related hearing loss while the tails of the tuning curve are almost intact. This is in contrast to the tuning curve associated with the OHC lesions where the tails were remarkably broadened. The IHC-related hearing loss (8 dB) is much smaller than the OHC-related hearing loss (25 dB) despite that the distribution of the hair cell damages in Figure 7A shows more IHC damages than OHC damages in this specific case. These simulations numerically confirm the common belief that the OHCs are more responsible for the threshold elevations than the IHCs

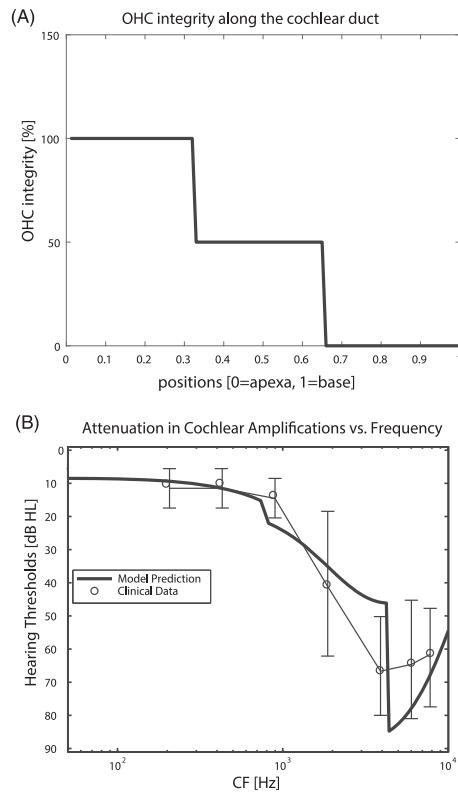


FIGURE 5 (A) A theoretical distribution of the outer hair cell (OHC) damages. (B) The model prediction for the hearing loss associated with the configuration in panel (A) is depicted at characteristic frequencies (CFs) from 0.1 to 10 kHz. The circles represent the average hearing thresholds at the corresponding frequencies obtained from the “sensory” panel in figure 2.13 of Schmiedt.³⁶ The error bars show the range of the expected values

(e.g., References 27, 37). Moreover, there is no horizontal shift in the tip of the IHC-damaged curve and the tails are also intact, unlike the tuning curve associated with the OHC damages where the horizontal shift of the tip and the broadening of the tails were substantial. Both of these phenomena are related to the active role of OHCs in cochlear mechanics. The reduction of active OHC forces leads to broadened filters and thereby a deficit in frequency selectivity. Moreover, OHC lesions cause changes in frequency-position tonotopic map of the cochlea due to the shift of best frequencies (BFs) toward apex. For example, Saremi and Stenfelt¹⁵ simulated these changes due to age-related decline of OHC forces.

3.4 | Phase locking in quiet and in background noise

Figure 8A shows the phase histogram assessed from the HSR AN spikes generated by the model in response to an 50-dB SPL tone at 1 kHz. The phase histogram illustrates the number of AN spikes per phase. Equation (1a) yields a mean phase of 1.49 [rad] (slightly below $\pi/2$) for this phase histogram meaning that the AN spikes averagely occur at the phase 1.49 [rad] of the stimulus. Furthermore, inserting the corresponding phase values in Equation (1b) yields a vector strength (r) of 0.73 for this phase histogram.

The vector strength (r) is similarly calculated in response to tones from 0.3 to 4 kHz for our model. The results are shown in Figure 8B along with the averaged experimentally assessed vector strengths on cat HSR AN fibers recorded by.³¹ Figure 8B indicates that the model predicts the decline of the vector strength with frequency in close agreement with these experimental data with only 0.055 MAE deviation. The model prediction deviates from the experimental data at frequencies higher than 2 kHz but it is important to note that phase locking patterns are more physiologically relevant at low frequencies where, according to Figure 8B, a very close match between model predictions and the experimental data is observed.

Figure 9 shows the phase locking of the HSR AN fibers to tones when there are mixed OHC/ IHC damages according to the configuration in Figure 7A. Figure 9A shows the decline of the phase locking for the healthy

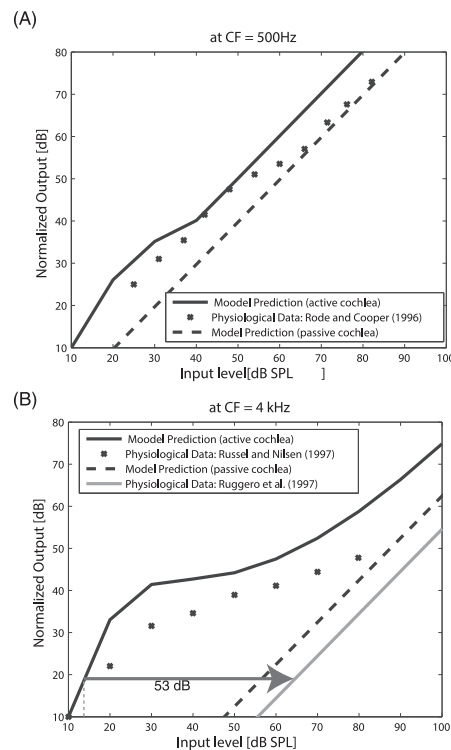


FIGURE 6 (A) The input/output (I/O) function estimated at 500 Hz (apical region of human cochlea) is normalized and shown by the solid line. The crosses depict the normalized I/O function recorded in the apical turn of the chinchilla cochlea.²³ The dashed line shows the model prediction of the I/O function when outer hair cells (OHCs) are dead in the entire cochlea. (B) The I/O function estimated at 4 kHz (basal region) is normalized and shown by the solid line. The crosses depict the normalized I/O function recorded in the comparable basal region of the guinea-pig cochlea.²⁶ The dashed line shows the model prediction of the I/O function when the OHCs are dead along with the I/O function of the postmortem chinchilla cochlea (gray solid line)²⁴

case and the pathological case and both curves are nearly identical. It suggests that the OHC/IHC damages have almost no negative effect on the phase locking pattern. This is in line with most experimental studies which found no significant negative impact of the NIHL on the phase locking in quiet (see Henry and Heinz³⁴ for a detailed review).

Figure 9B, however, shows the phase locking at the same frequency range for the healthy and pathological cases but in presence of a wide-band noise 15 dB above the tone level. Figure 9B shows that the phase locking is lower for both healthy (dashed line) and pathological (gray solid line) cases in the background noise compared to in quiet (black solid line). Moreover, the decline of the vector strength as a function of frequency is greater. Unlike the quiet background, in noise, the pathological condition results in a vector strength that is 0.05–0.1 lower than that of the healthy condition. This indicates that although the phase locking is substantially degraded by the background noise for both healthy and pathological conditions, it is more severe for the pathological condition.

Henry and Heinz³⁴ recorded spike trains on chinchilla AN fibers in response to tones in 42 normal-hearing cochleae versus 38 noise-induced cochleae and calculated the phase locking and the vector strength of the spikes. They found no significant difference between the phase locking of the AN spikes in healthy and pathological ears when tested in quiet. However, when playing the tones together with a 20-kHz wide-band noise 15 dB louder than the tone (similar to our methodology), they found that the phase locking is substantially impaired in the group with hair cell lesions (figure 2 of Henry and Heinz³⁴).

3.5 | Diagnosing OHC lesions

Figure 10A shows the averaged hearing thresholds of the seven male NIHL patients measured by standard audiometry at frequencies 0.125, 0.25, 0.5, 1, 1.5, 2, 3, 4, 6, and 8 kHz. The error bars represent the SD at each frequency. This

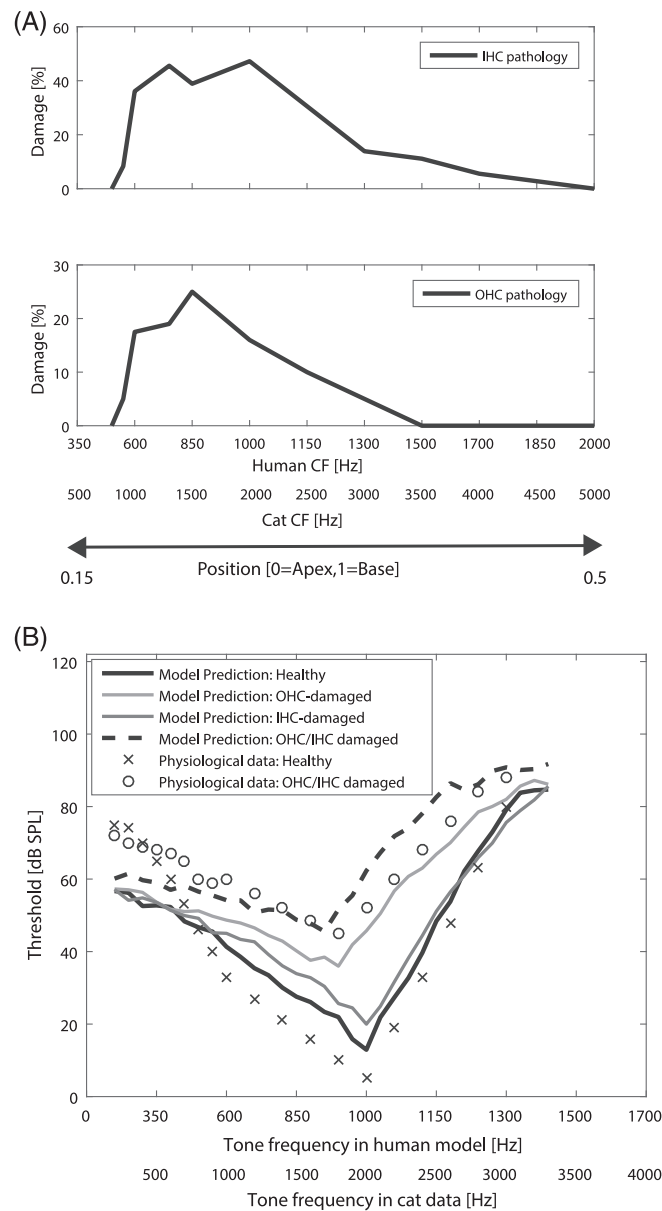


FIGURE 7 (A) The combined outer hair cell (OHC)/inner hair cell (IHC) pathologies reported by figure 4C of Liberman and Dodds.⁵ (B) The tuning curve estimated for the healthy condition (shown by the solid line) at the characteristic frequency (CF) of 1 kHz is accompanied by the tuning curves associated by combined OHC/IHC pathologies (dashed line). The tuning curves for the IHC pathology and the OHC pathology are also shown (gray lines). The corresponding physiological data recorded by Liberman and Dodds⁵ are reproduced and shown for the healthy case (crosses) and the OHC/IHC damaged case (circles)

audiogram is fed into the diagnosis algorithm and the model, based on Nelder–Mead optimization method, finds a configuration of OHC lesions across the cochlea that could generate the given audiogram. Figure 10B shows the OHC configuration found by the optimization method after 1000 iterations. It took about 22 min for this numerical algorithm to run 1000 iteration on an Intel[®] core[™] i5, 2.9-GHz personal computer. According to Figure 10, the OHCs in the base of the cochlea (most 35% basal area corresponding to CFs higher than 3.5 kHz) are substantially damaged whereas the OHCs in the middle of the cochlea (35%–70% of the cochlear length from base corresponding to CFs 0.5–3.5 kHz) are less damaged. The OHCs in the most apical region are totally intact.

The OHC configuration shown in Figure 10B is fed into the cochlear mechanics model and the cochlear amplification produced by the model at low-intensity sounds (i.e., $L = 30$ dB over the hearing threshold) is compared with the case wherein all OHCs are healthy. This predicts the threshold elevations associated with this particular OHC configuration. The result is shown by the solid line in Figure 10C which closely follows the given

input audiogram (dashed line). The MAE between the model output and the input audiogram is approximately 0.6 dB indicating the success of the optimization method in finding an OHC configuration that can result in hearing threshold elevations which can closely match the input audiogram. The code that generates Figure 10 can be found on GitHub.³⁹

Figure 11A shows the HINT results for the normal-hearing group versus the NIHL group. Figure 11B illustrates the phase locking of HSR AN fibers, in terms of vector strength, for the normal-hearing group versus NIHL group with the OHC lesions predicted by the optimization algorithm and shown by Figure 10B. These vector strength values were calculated in response to 50-dB SPL tones ranging from 0.25 to 4 kHz and in presence of noise. The background noise here is chosen 5 dB over the tone level (SNR = -5 dB) to resemble the SNR used in speech recognition tests (e.g., HINT). Figure 11B indicates that the NIHL group manifest a lower phase locking at low frequencies which declines quickly as the frequency of the tone increases. This suggests that the NIHL group might have problem in resolving temporal cues in sound signals due to deficits in phase locking^{4,37}

As illustrated in Figure 11A, the HINT scores for the NIHL group was found +0.2 dB (SD = 1.49) whereas it was -4.99 dB (SD = 0.91 dB) for a baseline of 20 normal-hearing individuals. HINT score estimates the amount of SNR that is needed for an individual to correctly recognize half of the words in the presented sentences. Therefore, our results suggest that the NIHL individuals averagely need approximately 5 dB higher SNR than normal-hearing individuals to obtain the same amount of speech recognition.

Therefore, to assess the contribution of phase-locking deficits to the observed speech recognition (HINT) results, the vector strengths were calculated at SNR = -4.99 dB for the healthy group and at SNR = +0.2 dB for the NIHL group and the results are shown in Figure 11C. Figure 11C indicates that, at these SNRs, the two groups depict similar phase locking capabilities at least at lower frequencies. This suggests that the 5-dB increase of SNR (from -4.99 to +0.2 dB) as inspired by the speech recognition test (HINT) has compensated the phase locking deficit in the NIHL group to a degree that it closely approaches the phase locking in the healthy group at least at lower frequencies (below 1 kHz). The two curves somewhat deviate at higher frequencies as NIHL curve (dashed) drops further below the healthy curve (solid).

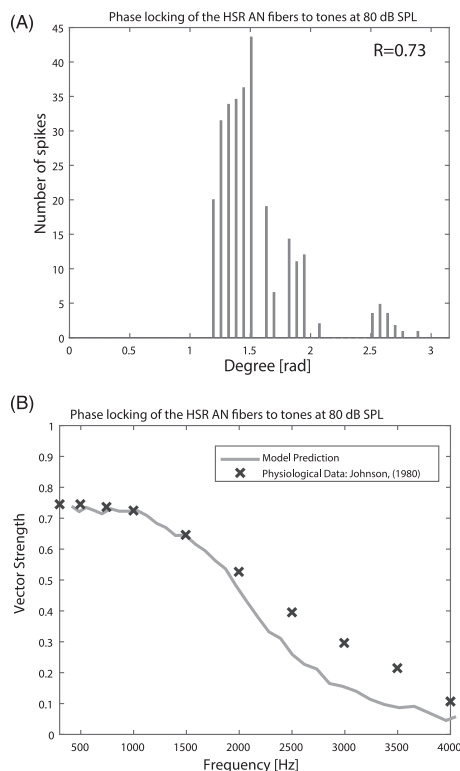


FIGURE 8 (A) The phase histogram of the auditory nerve (AN) firings shows the number of the AN spikes at different phases of the stimulus in response to a 50-dB SPL tone at 1 kHz. The corresponding vector strength is 0.73 according to Equation (1). (B) The vector strength is calculated for frequencies between 0.3 and 4 kHz for the presented model showing a decrease as a function of frequency. The crosses represent the physiological data recorded on the cat AN high spontaneous rate (HSR) fibers by Johnson³¹

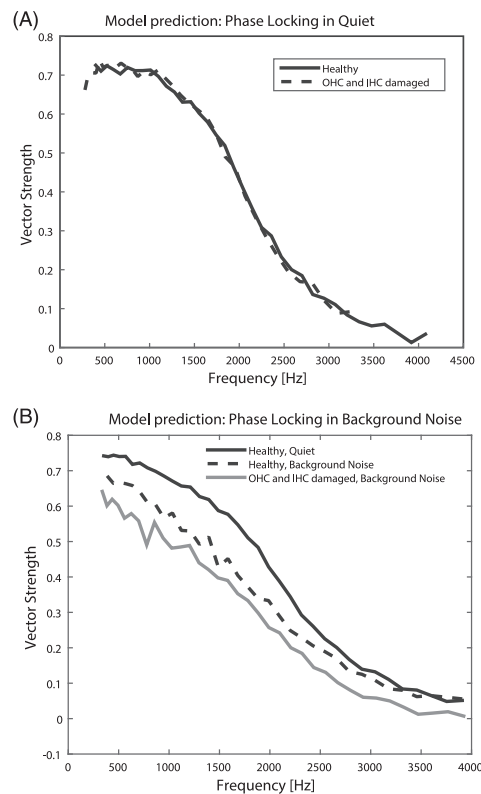


FIGURE 9 (A) The vector strength of the auditory nerve (AN) spikes in response to a 50 dB-SPL tone at frequencies from 0.3 to 4 kHz for the healthy condition versus the pathological condition. The distribution of the outer hair cell (OHC) and inner hair cell (IHC) damages used for these simulations are shown in Figure 7A. (B) The vector strengths are shown in presence of wide-band noise at root mean square (RMS) amplitude of 15 dB higher than that of the tone

Above 2 kHz, the gap between these two curves is as large as in Figure 11A suggesting that phase locking at higher frequencies is not compensated by increasing the SNR. However, these deviations may be physiologically irrelevant since phase locking concept is most valid at low frequencies (typically lower than 1 kHz).^{6,31–33} where the two curves closely match, indicating that the increase of SNR (inspired by HINT scores) has compensated the phase locking deficits in the NIHL group to a great extent.

4 | DISCUSSION

A detailed model of the mammalian cochlea was used to simulate the effects of specific noise-induced pathologies on the cochlear mechanics and the neuronal coding on the AN. The predictions of the model were evaluated by comparison with the corresponding animal data, whenever available, and the results were extrapolated to humans using the model. A particular aim of the simulations was to quantify and differentiate the effect of OHC and IHC pathologies on the spectral features of the cochlear responses.

The model consists of four stages, as seen in Figure 1 and described in Appendix, and a large number of cell-level parameters incorporated in a cascade configuration. This facilitates the simulation of the effects of cellular inner-ear lesions on the cochlear mechanics and, the spectral and temporal features of the peripheral coding on the AN. The effects of specific IHC and OHC lesions were simulated by means of scaling the OHC and IHC outputs in the corresponding partitions of the model. However, in principle, any of the 12 biophysical parameters characterizing the OHCs (listed in table II and table III of Saremi and Stenfelt¹⁵) or the 29 biophysical parameters of the IHC model (listed in table I of Lopez-Poveda and Eustaquio-Martin¹⁸) can be altered independently to study its consequences on the peripheral auditory functions. This is an important aspect that is beyond the realm of any phenomenological (functional) model which, per definition, aims to simulate the overall behaviors without getting directly involved with

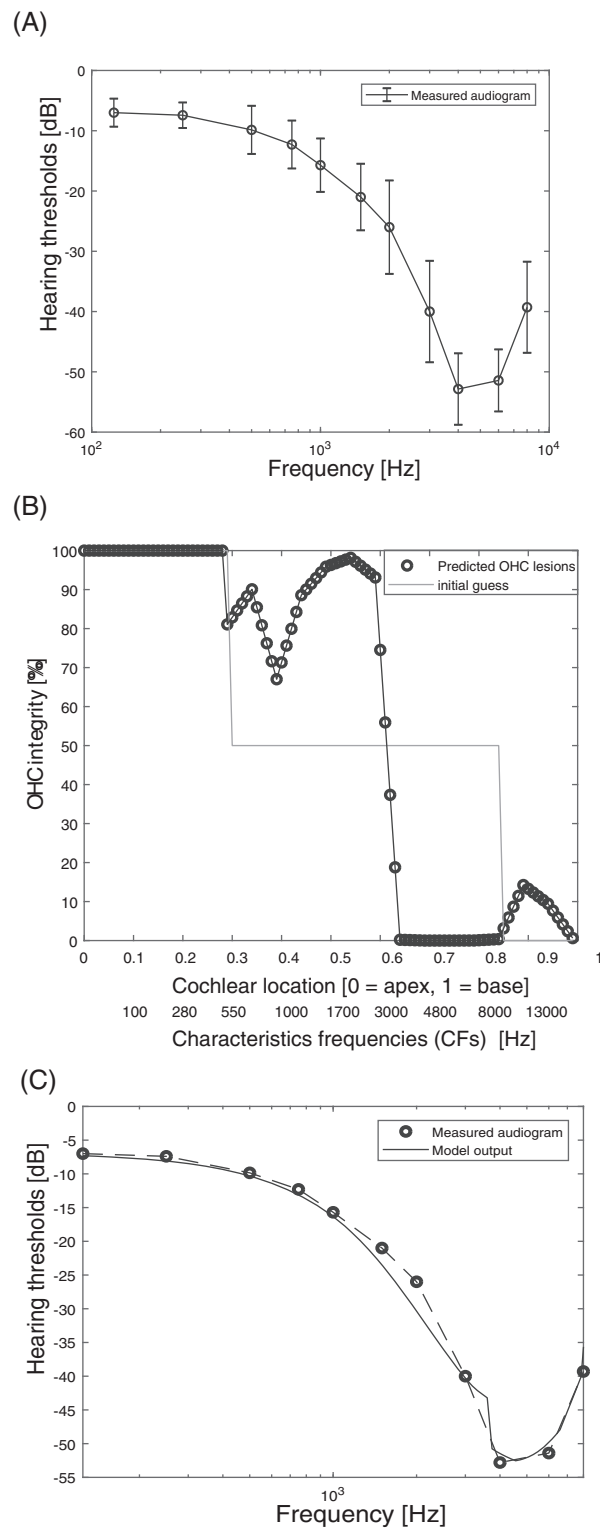


FIGURE 10 (A) The audiogram averaged from the audiometric hearing thresholds of seven individuals with documented noise-induced hearing loss (NIHL). The error bars illustrate the SDs. (B) The specific configuration of outer hair cell (OHC) lesions that the model associated with the given audiogram in (A). (C) The audiometric hearing loss predicted by the model for the OHC lesions shown in (B) versus the given audiogram in (A) depicting a close match

underlying biophysical parameters at the cellular level. Saremi and Stenfelt,¹⁵ for instance, used the cochlear mechanics stage of this biophysical model to simulate the effects of the age-related reduction of the endocochlear potential (one of the many parameters of the model) on the cochlear mechanical responses.

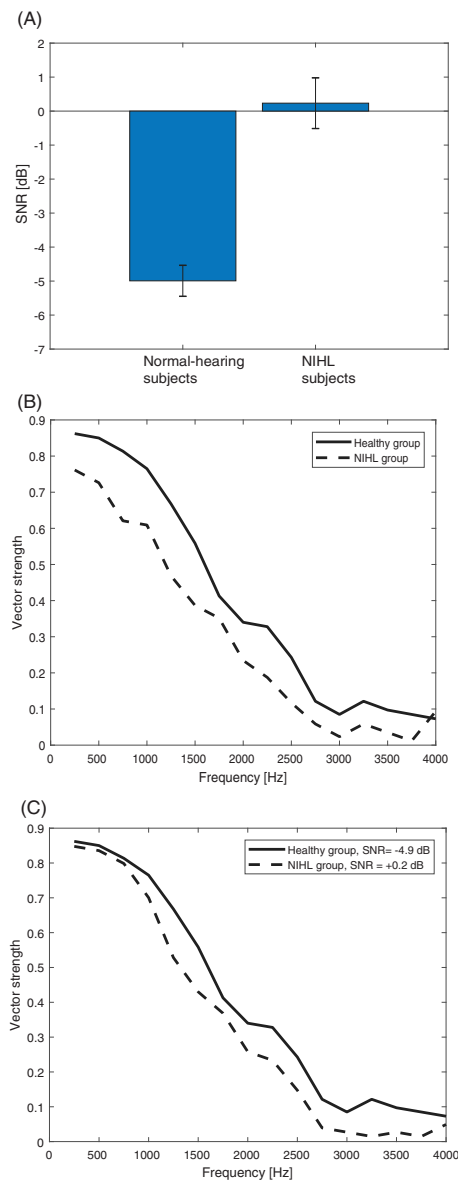


FIGURE 11 (A) The hearing-in-noise test (HINT) scores clinically assessed for the noise-induced hearing loss (NIHL) group versus the normal-hearing group. The error-bars represent the SDs. (B) Phase locking of high spontaneous rate (HSR) auditory nerve (AN) fibers in response to 50-dB SPL tones between 0.25 and 4 kHz in presence of wideband background noise at SNR = -5 dB. (C) Phase locking at SNR = -4.99 dB and SNR = $+0.2$ dB for the healthy and the NIHL groups, respectively

It takes 2.1 s for the presented model to generate AN spikes on the HSR fibers in response to a tone fed into its input, using a regular Intel[®] core[™] i5, 2.9-GHz personal computer. Saremi et al.¹³ reported the computational costs for a number of cochlear mechanics models in their table IV, and showed that it might take a shorter time for simpler models with fewer parameters to process an incoming tone. It is, however, the nature of the application at hand and the available computational resources which determines whether the use of a more detailed biophysical model is reasonable.

In this study, we simulated the effects of specific OHC and IHC lesions, caused by acoustic overstimulation, on the hearing threshold, cochlear mechanical compression, as well as the cochlear spectral coding (neuronal tuning curves) and temporal coding (AN phase locking). The simulation results were compared to measurements from corresponding proportional locations on other mammalian cochleae.

The hearing thresholds were estimated according to the neuronal activity on the HSR auditory fibers. Our definition of threshold was a tone level that generates a 10% increase in the firing rate of the HSR AN compared to its baseline spontaneous rate. Some experimental studies, for example, References 5, 21 and modelers, for example,

References 19, 22 used an absolute threshold definition (i.e., a tone level that yields 10 spikes over the spontaneous baseline). Given the baseline spontaneous rates, these two definitions are nearly the same. However, we learned through our simulations that a percentage-based definition helps control the numerical noise and leads to more stable responses. Liberman²¹ hypothesized also that the “threshold spread would be somewhat less” if a percent-based criterion was used. The simulations showed a close match with the corresponding thresholds measured in cats, as seen in Figure 2, with MAE deviation of 2.5 dB across the frequency range (0.3–10 kHz). The hearing thresholds were also estimated for cases with selective IHC and OHC pathologies and were shown in Figures 3 and 4, respectively. The simulation results were in line with the corresponding experimental data^{5,27} with MAEs of 0.4 and 4.1 dB, respectively.

Moreover, a theoretical distribution of the noise-induced OHC damages on the cochlear length was assumed (Figure 5A). The hearing loss associated with this theoretical distribution of OHC lesions was shown to be within the range of the “sensory” hearing loss phenotype assessed from a 188-audiogram database in a human clinical study.³⁶ To further examine the capabilities of the model in linking underlying cochlear lesions to given audiograms, an optimization algorithm based on Nelder–Mead method was developed. Standard audiometry was performed on a group of seven individuals with documented NIHL and the averaged audiogram was used as the input. The optimization algorithm found a specific OHC configuration that results in hearing threshold elevations that closely match with the given audiogram. This information might be very valuable for diagnostic purposes which aim to associate an observed clinical outcome to specific underlying cochlear lesions that could have caused it.

An alternative method is to feed the seven audiograms into the optimization algorithm individually and thereafter average the estimated OHC lesion patterns. Our simulations show that this latter method yields a different OHC pattern from what is shown in Figure 10B and that the final audiogram re-generated by this alternative method is not as close to the input audiogram as shown in Figure 10C. Therefore, the method described here (i.e., averaging the seven audiograms before feeding to the optimization algorithm) is more accurate in terms of reproducing the clinical data. The differences in the outcomes of these two methods could be due to variations in the individual audiograms that are minimized by averaging them before feeding into the optimization algorithm.

The fundamental assumption for these simulations is that OHC lesions are the only source of the hearing threshold elevations. This assumption is taken to be able to focus on one set of optimization variables. Although OHC lesions are known to be the primary reason for hearing threshold elevations in NIHL,³⁷ other underlying factors such as EP reduction (due to aging), and IHC lesions can be present in real world cases. If so, these parameters can be also included in the optimization algorithm to produce OHC, IHC, and EP configurations which can result in the given hearing threshold elevations. Including these factors was beyond the scope of the current paper and we solely focused on OHC lesions to simplify the process from a computational point of view. These factors could be included in the simulations in future studies.

The tuning curve was estimated at the CF of 1 kHz for the healthy condition, as well as for a pathological case with combined IHC/OHC lesions (figure 4C of Liberman and Dodds⁵). The amount of tip elevation predicted by the model (33 dB) was in the same order as the tip elevation of the corresponding measured tuning curve⁵ (i.e., 40 dB). Furthermore, to differentiate between the OHC and IHC contribution to the changes in the tuning curve, the tuning curve was estimated separately for OHC pathologies and IHC pathologies. The results indicated that, although the IHC damage was more spread and prominent than the OHC damage, the OHC-related tip elevation was 25 dB whereas the IHC-related tip elevation accounted for only 8 dB of the total elevation. This suggests that the spectral coding of the cochlea is more vulnerable to damages to OHCs than IHCs since a lesser OHC lesion leads to greater tip elevation and broadening of the cochlear neuronal tuning curve.

In contrast, our results suggested that IHC and OHC pathologies might not modify the phase locking pattern in quiet. Our simulations, however, indicated that the vector strength of the AN spikes is substantially lower in presence of noise for both healthy and pathological conditions but the decline of the phase locking is more prominent in a cochlea with IHC/OHC lesions. The observed negative effect of the background noise on the temporal coding can be attributed to the broadening of the auditory filters.

Broader cochlear tuning allows more noise energy to enter the corresponding auditory channel and increases the number of spikes driven by noise rather than by the tone. As the hair cell lesions, especially damages to OHCs, lead to substantial broadening of the tuning curves (see Figure 7B), the listeners with hair cell pathologies have a poorer temporal coding and more difficulty in presence of noise than the normal hearing listeners.³⁴ Our HINT results clinically showed that the NIHL group need about 5 dB higher SNR than the normal-hearing baseline to be able to demonstrate similar performance in speech understanding tasks. Figure 11C showed that a 5-dB

increase in SNR improves the phase locking in the NIHL group (with predicted lesions shown in Figure 10B) and, to some degree, compensates the phase locking deficits at least at the most interesting frequencies which are lower than 1 kHz.

Although our simulation results generally showed good agreement with the available experimental data, some deviations between the model predictions and the corresponding experimental data can be observed in a number of cases such as in Figures 6, 7B, and 8B. A major source of such discrepancies is the limitations in the existing measurement techniques. Measuring inside a living cochlea is a complicated procedure and is usually accompanied by many practical assumptions which are not without inaccuracies. Moreover, the translational nature of the data used in this study contributes to further inaccuracies and discrepancies between model outcomes and experimental data. Although mammalian cochleae share relatively similar mechanics at proportionally similar locations in the cochlear duct, there are still species-specific differences among mammalian cochleae, considering their diverging evolutionary paths, which generates inaccuracies in the translational data used in this study. Furthermore, we used AN data in so far as available to compare with our AN model. However, in few cases such as in Figures 3 and 4, CAP and ABR thresholds were respectively used due to their availability. Although CAP and ABR hearing thresholds have been shown to have a very close correlations with AN-based thresholds,⁴⁰ there are apparently differences which would inevitably impose inaccuracies in our comparisons.

Another source for the observed discrepancies is inaccuracies in the model itself. The discrepancies between model predictions and the data in each task could be minimized by re-tuning some specific parameters in the model. However, such targeted parameter tuning could cause “over-tuning” toward one specific task. A computational model, regardless of its complexity, is still a simplification of the natural processes involved. As a general rule, a model that can modestly reproduce the experimental data across a spectrum of several tasks is considered more successful and reliable than a model that can reproduce the data very closely in a few tasks whereas substantially deviating from the experimental data in some other tasks.

The focus of this study was the noise-induced hair cell lesions and their effects on the cochlear functions. Liberman and Kujawa⁴ experimentally showed that, besides of the hair cells, the acoustic overstimulation might also affect other auditory structures and cause acute loss of afferent terminals and the structural degeneration of the AN itself which can contribute to additional impairments in the temporal coding of sounds. Although, it was shown that such impairment could minimally affect the hearing thresholds.³⁷ Simulating the effect of such noise-induced nerve terminal impairments on more complex tasks such as speech perception requires adding the responses of AN populations as well as modeling more central parts of the auditory system. This suggests that there is still a long way to fully understand the biophysics of the noise-induced cochlea.

5 | CONCLUSION

The effects of selective noise-induced IHC and OHC damages on the peripheral auditory functions were simulated using a detailed biophysically motivated model. Several configurations of OHC and IHC pathologies were retrieved from published animal data. The effects of these pathologies on the hearing thresholds (defined according to the HSR AN fiber activity) were simulated for a wide range of frequencies. The cochlear nonlinear response growth was assessed by estimating the I/O functions at 500 Hz (apical area) and at 4 kHz (basal area) of the human cochlea.

A case of mixed OHC/IHC pathologies was retrieved from the cat data and used to simulate the tuning curves. Besides, the IHC and OHC contribution to the tip elevation of the tuning curve were differentiated and analyzed by the model. The phase locking of the AN spikes in response to tones were assessed both in quiet and in presence of background noise. The model predicts that the phase locking is drastically deteriorated in noisy background especially for the pathological condition.

The presented results manifest that a biophysical modeling approach is suitable for simulating noise-induced hair cell pathologies as the model could predict animal data from cat, chinchilla, and guinea pig. The model, as a theoretical framework, allows rationally extrapolating these animal data to equivalent locations in the human cochlea to better understand the consequences of given noise-induced cellular lesions on the auditory functions. Vice versa, an optimization algorithm was developed to enable the model to find a specific configuration of noise-induced OHC lesions that could have caused an audiogram measured in a group of individuals with known NIHL. This suggests that the presented biophysically motivated modeling approach can be useful for relating a given individualized clinically observed deficit of the auditory functions to specific cellular lesions in the inner ear and, thereby, provide important diagnostic information on an individual basis.

ACKNOWLEDGMENTS

This research was supported by the Swedish Research Council (349-2007-8654, and 2017-06092), Hörselskadades Riksförbund (HRF), and by the DFG Cluster of Excellence EXC 1077/1 “Hearing4all,” University of Oldenburg, Germany. The clinical data collection was performed at the hearing clinic at Linköping University Hospital.

DATA AVAILABILITY STATEMENT

The data that support the findings of this study are openly available in Github at <https://github.com/AminSaremi/CochlearMechanics-model>.

REFERENCES

1. Lydia MH, Kamenov K, Briant PS, et al. Hearing loss prevalence and years lived with disability, 1990–2019: findings from the Global Burden of Disease Study 2019. *Lancet*. 2021;397(10278):996-1009.
2. Cody AR. Acoustic lesions in the mammalian cochlea: implications for the spatial distribution of the ‘active process’. *Hear Res*. 1997;62:166-172.
3. Lim HW, Choi SH, Kang HH, Ahn JH, Chung JW. Apoptotic pattern of cochlear outer hair cells and frequency-specific hearing threshold shift in noise-exposed BALB/c mice. *Clin Exp Otolaryngol*. 2008;1(2):80-85.
4. Liberman CM, Kujawa SG. Cochlear synaptopathy in acquired sensorineuronal hearing loss: manifestations and mechanisms. *Hear Res*. 2017;349:138-147.
5. Liberman CM, Dodds LW. Single-neuron labeling and chronic cochlear pathology III. *Hear Res*. 1984;16:55-74.
6. Fettiplace R, Hackney CM. The sensory and motor roles of auditory hair cells. *Nat Rev Neurosci*. 2006;7:19-29.
7. Pyykkö I, Strack J, Toppila E, Ulfendahl M. Noise-induced hearing loss. In: Luxon L, ed. *Textbook of Audiological Medicine: Clinical Aspects of Hearing and Balance*. Taylor and Francis Group; 2006:477-494.
8. Stenfelt S. Towards understanding the specifics of cochlear hearing loss: a modelling approach. *Int J Audiol*. 2008;47(2):5-10.
9. Stenfelt S, Ronnberg J. The signal-cognition interface: interactions between degraded auditory signals and cognitive processes. *Scand J Psychol*. 2009;50:385-393.
10. Lopez-Poveda EA, Johannesen PT. Behavioral estimates of the contribution of inner and outer hair cell dysfunction to individualized audiometric loss. *J Assoc Res Otolaryngol*. 2012;13(4):485-504.
11. Kujawa SG, Liberman CM. Adding insult to injury: cochlear nerve degeneration after temporary noise-induced hearing loss. *J Neurosci*. 2009;29(45):14077-14085.
12. Meddis R, Lopez-Poveda EA. Peripheral auditory system: from pinna to auditory nerve. *Computer Models of the Auditory System*. Springer; 2010:7-38.
13. Saremi A, Beutelmann R, Dietz M, Ashida G, Kretzberg J, Verhulst S. A comparative study of seven human cochlear filter models. *J Acoust Soc Am*. 2016;140:1618-1634.
14. Liu YW, Neely ST. Outer hair cell electromechanical properties in a nonlinear piezoelectric model. *J Acoust Soc Am*. 2009;126:751-761.
15. Saremi A, Stenfelt S. Effects of metabolic presbycusis on cochlear responses: a simulation approach using a physiologically-based model. *J Acoust Soc Am*. 2013;134(4):2833-2852.
16. Meaud J, Lemons C. Nonlinear response to a click in a time-domain model of the mammalian ear. *J Acoust Soc Am*. 2015;138(1):193-207. doi:10.1121/1.4921282
17. Nelder JA, Mead R. A simplex method for function minimization. *Comput J*. 1965;7(4):308-313.
18. Lopez-Poveda EA, Eustaquio-Martin A. A biophysical model of the inner hair cell: the contribution of potassium currents to peripheral auditory compression. *J Assoc Res Otolaryngol*. 2006;7:218-235.
19. Zilany MS, Bruce IC, Carney LH. Updated parameters and expanded simulation options for a model of the auditory periphery. *J Acoust Soc Am*. 2014;135:283-286.
20. Goode RL, Killion M, Nakamura K, Nishihara S. New knowledge about the function of the human middle ear: development of an improved analog model. *Am J Otol*. 1994;15:145-154.
21. Liberman MC. Auditory-nerve response from cats raised in a low-noise chamber. *J Acoust Soc Am*. 1978;63(2):442-455.
22. Zilany MSA, Bruce IC. Modeling auditory-nerve responses for high sound pressure levels in the normal and impaired auditory periphery. *J Acoust Soc Am*. 2006;120(3):1446-1466.
23. Rhode WS, Cooper NP. Nonlinear mechanics in the apical turn of the chinchilla cochlea in vivo. *Audit Neurosci*. 1996;3:101-121.
24. Ruggero MA, Nola CR, Recio A, Narayan SS, Robles L. Basilar membrane responses to tones at the base of the chinchilla cochlea. *J Acoust Soc Am*. 1997;101(4):2151-2163.
25. Robles L, Ruggero MA. Mechanics of the mammalian cochlea. *Physiol Rev*. 2001;81:1305-1352.
26. Russel IJ, Nilsen KE. The location of the cochlear amplifier: spatial representation of a single tone on the Guinea pig basilar membrane. *Proc Natl Acad Sci USA*. 1997;94:2660-2664.
27. Wang J, Powers NL, Hoffstetter P, Trautwein D, Ding RS. Effects of selective inner hair cell loss on auditory nerve fiber threshold, tuning and spontaneous and driven discharge rate. *Hear Res*. 1997;107:67-82.
28. Glasberg BR, Moore BCJ. Derivation of auditory filter shapes from notched-noise data. *Hear Res*. 1990;47:130-138.
29. Sek A, Alcantara J, Moore CJ, Kluk K, Wicher A. Development of a fast method for determining psychophysical tuning curves. *Int J Audiol*. 2005;44:408-420.

30. Patterson RD, Moore BCJ. Auditory filters and excitation patterns as representations of frequency resolution. *Frequency Selectivity in Hearing*. Academic; 1986:123-177.
31. Johnson DH. The relationship between spike rate and synchrony in responses of auditory nerve fibers to tones. *J Acoust Soc Am*. 1980; 68:1115-1122.
32. Goldberg JM, Brown PB. Responses of binaural neurons of dogs superior olivary complex to dichotic stimuli. *J Neurophysiol*. 1969;32(4):613-636.
33. Köppl C. Phase locking to high frequencies in the auditory nerve and cochlear nucleus magnocellularis of the barn owl. *Tyto alba. J Neurosci*. 1997;17(9):3312-3321.
34. Henry K, Heinz MG. Effects of sensorineuronal hearing loss on temporal coding of narrow-band and broadband signals in the auditory periphery. *Hear Res*. 2013;303:39-47.
35. Greenwood DD. Comparing octaves, frequency ranges, and cochlear-map curvature across species. *Hear Res*. 1990;94(1996):157-162.
36. Schmiedt RA. Physiology of cochlear presbycusis. *The Aging Auditory System*. Springer Science+Business Media; 2010, 2010:9-38.
37. Oxenham AJ. Predicting the perceptual consequences of hidden hearing loss. *Trends Hear*. 2016;20:233121651668676. doi: [10.1177/2331216516686768](https://doi.org/10.1177/2331216516686768)
38. Hällgren M, Larsby B, Arlinger S. A Swedish version of the hearing in noise test (HINT) for measurement of speech recognition. *Int J Audiolog*. 2006;45:227-237.
39. Saremi A. Cochlear mechanics model. *Github*. Accessed November 25, 2021. 2021; <https://github.com/AminSaremi/CochlearMechanics-model>
40. Munnerly GM, Greville KA, Purdy SC, Keith WJ. Frequency-specific auditory brainstem responses relationship to behavioural thresholds in cochlear-impaired adults. *Audiology*. 1991;30(1):25-32.
41. Békésy GV. *Experiments in Hearing*. McGraw-Hill; 1960:403-703.
42. Zweig G, Lipes R, Pierce JR. The cochlear compromise. *J Acoust Soc Am*. 1976;59:975-982.
43. Lopez-Poveda EA. Auditory computation and psychoacoustics. *Available*. 2020. <http://audiolab.usal.es/> (Last viewed 15/12/2021).
44. Søndergaard P, Majdak P. The auditory modeling toolbox. *The Technology of Binaural Listening*. Springer; 2013:33-56.
45. Zhang X, Heinz MG, Bruce IC, Carney LH. A phenomenological model for the responses of auditory-nerve fibers: I. Nonlinear tuning with compression and suppression. *J. Acous. Soc. Am*. 2001;109:648-670.

How to cite this article: Saremi A, Stenfelt S. The effects of noise-induced hair cell lesions on cochlear electromechanical responses: A computational approach using a biophysical model. *Int J Numer Meth Biomed Engng*. 2022;38(5):e3582. doi:[10.1002/cnm.3582](https://doi.org/10.1002/cnm.3582)

APPENDIX

THE BIOPHYSICAL CASCADE LUMPED-ELEMENT MODEL OF HUMAN COCHLEAR MECHANICS

The incoming acoustic pressure field causes the stapes to vibrate, resulting in a traveling wave along the organ of Corti propagating from the base toward the apex.⁴¹ The cascade modeling approach is based on the Wentzel-Kramers-Brillouin (WKB) method for simulating the wave propagation mechanics in a one-dimensional non-uniform media.⁴² According to this method, the response at any location along the cochlear duct can be approximated by composing a series of cascade media, each one with specific local parameters as if the medium were uniform. This cascade topology closely represents the “traveling wave” mechanics observed by Békésy.⁴¹ It is opposed to the simplified topology of the conventional parallel filterbank models that consist of discrete filterbanks which are excited independently by common stimuli. A comprehensive comparative study of several cochlear mechanics models (table III of Saremi et al.¹³) showed that cascade models are generally more accurate and successful in reproducing the experimental data.

Saremi and Stenfelt¹⁵ developed a biophysical lumped-element model that comprises a series of cascade resonators each of which represents a cochlear partition. In what follows, a short overview of the model and the changes that have been applied to it are presented.

Figure A1 below depicts a single cochlear partition of the model along the cochlear duct. It comprises three passive mechanical loads: the basilar membrane (BM), the reticular lamina (RL), and the tectorial membrane (TM). Here, each passive mechanical load (BM, RL, and TM) is modeled by a viscous “mass-spring-damper” combination, together with a spring-damper combination (shown by K_h and R_h in Figure A1) that models the longitudinal coupling between the partitions, extending from the base (left) to the apex (right). This structural longitudinal coupling between the partitions, however, leads to mathematical complexity due to the loading effect of the cochlear partitions on each other. This is not the case for the transmission-line and the cascade-filterbank configurations which generally assume that the longitudinal coupling is solely via the incompressible fluid

The OHCs lie between the RL and the BM; they produce motile forces (depicted by the pair force f_{OHC} in Figure 1) which, on a cycle-to-cycle basis, alternately pull the RL and the BM together and push them apart (figure 2 of Saremi and Stenfelt¹⁵) and hence add active force/energy into the transmission line. This additive behavior is included in the model by means of two feed-forwards both on the BM and the RL (Figure A1B). The OHC transfer function is integrated into the transmission line by a pair of positive feed-forwards both on the BM and on the RL as seen in Figure A1B.

From another perspective, this biophysical model links the cochlear vibrations to the underlying cell-level parameters since it consists of several parameters that have been directly extrapolated from detailed physiological experiments inside the mammalian cochlea, in so far as known. These parameters are listed in tables I, II, and III of Saremi and Stenfelt.¹⁵ This level of biophysical details allows simulating the effect of small changes in any of these detailed parameters on the overall cochlear responses. For instance, Saremi and Stenfelt¹⁵ investigated the effects of age-related EP reduction on the cochlear responses using the model. The MATLAB implementation of this model is publicly available on GitHub.³⁹

THE BIOPHYSICAL LUMPED-ELEMENT MODEL OF THE IHC

The IHC model used here was a biophysical model developed by Lopez-Poveda and Eustaque-Martin.¹⁸ The model consists of cell-level parameters such as the EP, capacitance and conductance of the cell portions, and the mechanical sensitivity of the potassium channels. These parameters are incorporated in an electrical-circuit equivalent of an IHC which gives the IHC membrane potential in its output, as a function of the stereocilia displacement caused by the cochlear vibrations.

The parameters of the model and its structural details are described by Lopez-Poveda and Eustaque-Martin.¹⁸ The model was shown to be capable of reproducing the experimental data, such as the IHC membrane potential responses (both DC and AC components) in response to the deflection of the IHC stereocilia. The MATLAB implementation of this IHC model is publicly available.⁴³

THE PHENOMENOLOGICAL MODEL OF AN RESPONSES

Based on some earlier works,⁴⁵ Zilany and Bruce^{19,22} introduced a parallel filterbank model to simulate the responses of the high spontaneous rate (HSR) auditory nerve fibers. This is achieved by two modes of the BM mechanical excitation to the inner hair cell (IHC), rather than one, based on a two-factor cancellation hypothesis whose biophysical correlates are unknown. The model comprises independent channels (parallel filterbanks) that are excited independently by the common input. This modeling strategy is based on the Helmholtz theory of “tuning forks,” in which the organ of Corti is viewed as a number of spatially ordered independent resonators, excited independently by a sound stimulus. This fundamental assumption simplifies the geometry of the model and results in significantly less computational costs.

In the Zilany AN model, cochlear vibrations are passed to a low-pass filter (mimicking the IHC), a model of the IHC-AN synapse, and eventually a spike generator. The parameters of the model were tuned primarily according to the cat auditory fiber responses. However, the model was also shown to reasonably reproduce the outcome of psychoacoustic experiments such as two-tone suppression experiments. The MATLAB and C implementation of the Zilany model are available at the AMtoolbox.⁴⁴

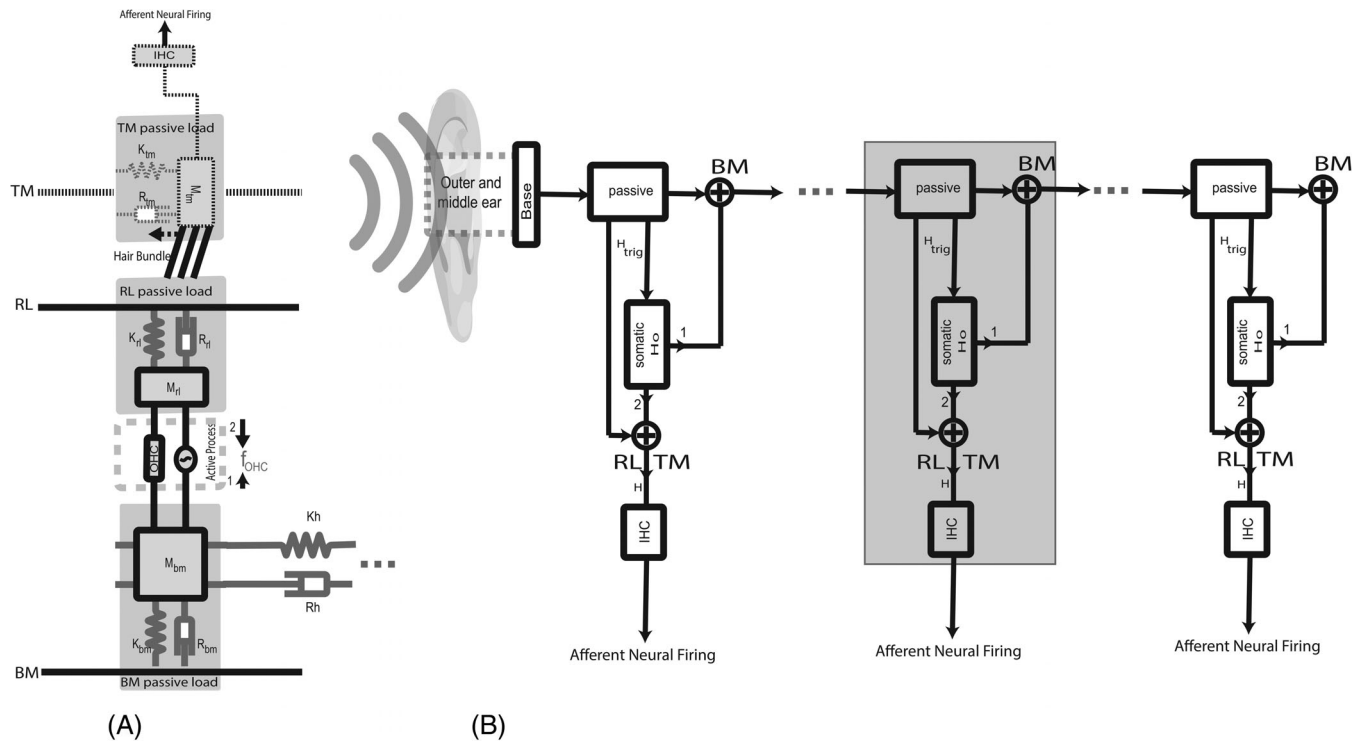


FIGURE A1 (A) A cochlear partition along the cochlear duct. It comprises three passive loads: the BM, the RL, and the TM which are each represented by a classic “mass-spring-damper” combination. The outer hair cell (OHC) is the active element which acts between the RL and the BM by applying motile forces (denoted by f_{OHC}). The vibration is transmitted to the IHC via the RL-TM shearing. If the x-coordinate corresponds to the longitudinal direction, RL and BM vibrate in x-z plane whereas TM shear motion is in the y-z plane and thus the corresponding elements are illustrated by dotted lines. The longitudinal coupling along the cochlear structures is modeled by a damper (R_h) and a spring (K_h). (B) A schematic of the lumped-element model. It consists of N discrete partitions which extend from the stapes (left) to the apex (right) forming a signal transmission line